

Saturation of the second harmonic generation from GaAs-filled metallic hole arrays by nonlinear absorption

Jingyu Zhang,¹ Li Wang,¹ Sanjay Krishna,¹ Mansoor Sheik-Bahae,² and S. R. J. Brueck^{1,*}

¹*Center for High Technology Materials and Department of Electrical and Computer Engineering, University of New Mexico, 1313 Goddard SE, Albuquerque, New Mexico 87106, USA*

²*Department of Physics and Astronomy, University of New Mexico, 800 Yale Boulevard NE, Albuquerque, New Mexico 87131, USA*

(Received 19 August 2010; revised manuscript received 31 January 2011; published 25 April 2011)

Saturation of the enhanced second harmonic generation (SHG) based on the localized fields confined in a nanoscale periodic, GaAs-filled, plasmonic structure is presented. The SHG saturates at high pump intensities due to three-photon absorption and the resultant free-carrier absorption. Free carriers are monitored by photoluminescence (PL). A fifth power dependence of the PL is observed at 297 K, which results from the three photon absorption along with a transition from nonradiative carrier recombination at the defected GaAs surface at low excitation to bimolecular recombination at high carrier concentrations.

DOI: [10.1103/PhysRevB.83.165438](https://doi.org/10.1103/PhysRevB.83.165438)

PACS number(s): 78.67.Pt

I. INTRODUCTION

Surface plasma wave (SPW) based integrated optical circuits, combining the speed and capacity of photonic circuits with the small size of electronic circuits, have attracted tremendous interest. SPWs are electromagnetic waves coupled to charge oscillations at a metal-dielectric interface. Their combined nature as part material excitation and part optical field enables localized control of electromagnetic fields at sub-wavelength scales.¹ The linear optical properties of periodic structures, fabricated on dielectric or semiconductor substrates with unit cell dimensions less than the wavelength of incident light, have been investigated extensively.^{2–6} Nonlinear optics resulting from the plasmonic structure, especially second harmonic generation (SHG), has also been investigated by combining the asymmetric character of the metal/dielectric interface with the enhanced localized field intensity coupled by SPWs.^{7–13} M. Wegener *et al.* also observed SHG from split-ring resonators on a GaAs substrate with (100) and (110) orientation.¹⁴ However, the detected SHG signals from an unstructured metal surface or only the interface of a metal and a nonlinear material are weak and while of scientific interest, hold little practical applicability. Conventionally, optical nonlinearities require long path lengths along with a phase matching scheme to allow coherent addition of contributions along the entire path, for example LiNbO₃, KTP, and BBO crystals to achieve applicable nonlinear signals with $\sim 30\%$ conversion efficiency. The problem is that cm-path interaction lengths are inherently inconsistent with microscale/nanoscale semiconductor devices. GaAs and related III-V materials are isotropic semiconductors with a large $\chi^{(2)}$ ($\chi^{(2)} = 2d$), for example, d_{14} (GaAs) $\approx 5 \times d_{33}$ (LiNbO₃) = 94 pm/V (near 4 μm) (Ref. 15) that have great potential as midinfrared nonlinear optical materials along with a capability for semiconductor integration. However, the phase mismatch between fundamental light and SHG signal still limits the conversion efficiency. Conventional phase-matching schemes are not possible for the cubic zinc-blende symmetry and current interest has evolved toward periodic poling, but still with macroscopic path lengths.¹⁶

We previously reported SHG resulting from a nanopatterned nonlinear material (GaAs) located inside the subwavelength holes of metallic hole and annular arrays.^{17,18} The experimental and theoretical analyses of linear transmission spectra and SPW-enhanced local fields have been presented. GaAs belongs to crystal point group $\bar{4}3m$. The symmetry properties of the group require that the radiating SH polarization component is perpendicular to that of incident light, as expressed by Eq. (1), and is proportional to the z -directed field strength. Thus the high-intensity z -directed fields play an important role in the observed SH signal. No SHG is observed from the same structure with Si replacing the GaAs because Si is an inversion-symmetric crystal structure without a bulk second-order nonlinear coefficient. The SH signal from an air-hole sample on a GaAs substrate is about ten times weaker than that of holes filled with GaAs. Therefore, the strongly enhanced electromagnetic fields in the vicinity of the patterned metal-dielectric interface materials, results in SHG from the very thin GaAs post area embedded in the Au film.^{17,18} Since the nonlinear interaction is confined to a very thin region $\sim 100 \text{ nm} \ll \lambda/n$, phase matching is not required.

The fabrication of the sample by interferometric lithography (IL) has been described in detail in Ref. 17. The structure consists of a two-dimensional (2D) Au hole array, with GaAs extending through the holes in the Au film, on a double polished semi-insulating (100) GaAs wafer. The linear transmission spectra of GaAs-filled metallic hole arrays were measured and simulated. In Ref. 17, the structure geometrical parameters were 879-nm pitch, 214-nm hole radius, 110-nm GaAs post height, and 65-nm thick Au layer. The first order SPW is at 3 μm , which can be easily calculated by a kinetic (momentum conservation) model.^{1,6} The first order transmission peak, associated with localized modes of the holes coupled by the first order SPW, is at 3.18 μm . The fields for the annular unit cell at the metal/air interface are strongly enhanced. The in-plane fields in the gap region are roughly comparable enhanced (approximately three or four times) to the incident field while the out-of-plane, z -directed fields are approximately ten times larger.

In this paper, we continue the investigation of the SHG of the subwavelength plasmon coupled GaAs hole arrays at

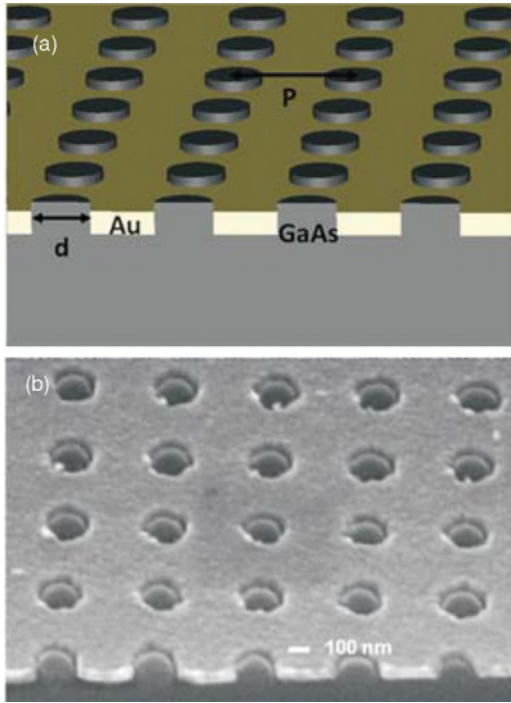


FIG. 1. (Color online) (a) Schematic of the plasmon-coupled GaAs structure consisting of GaAs posts extending through holes in Au film arrays (540-nm pitch; 220-nm diameter) on top of GaAs substrate. (b) SEM picture of the fabricated structure.

much higher pump intensities and with a somewhat scaled structure to shift the SPW resonance to $2.19 \mu\text{m}$. We confine our investigation to a hole array structure, instead of annular array structure, due to higher observed SHG signals and the much simpler fabrication. The geometrical parameters in this work are 540-nm pitch, 220-nm hole diameter, 110-nm height of GaAs posts, and 100-nm Au thickness, as shown in Fig. 1, shifting the SPW resonance to $2.1 \mu\text{m}$. The unit cell includes one GaAs post. The maximum first order SPW coupling (transmission dip) is at $1.88 \mu\text{m}$ and the coupled first order transmission peak is at $2.19 \mu\text{m}$. With x -polarized incident light, the E_x field intensity on the Au/(GaAs substrate) interface is enhanced ~ 1.5 times within the Au aperture compared to the incident field. The scattered E_z field is ~ 14 times enhanced at the edges of the GaAs posts, which gives the

dominant contribution to the SHG [see Eq. (1)]

$$P_{x,y}(2\omega) \propto \chi_{14}^{(2)}(2\omega; \omega, \omega) E_{y,x}(\omega) E_z(\omega). \quad (1)$$

Experimental and theoretical results of SHG saturation associated with nonlinear carrier generation and the associated free-carrier absorption are observed and discussed. We find that the second harmonic (SH) signal is strongly enhanced compared to that of a bulk GaAs substrate at normal incidence. As noted above, we have previously compared the SHG with that of an unpatterned GaAs substrate and a comparable SPW structure, and found about an order of magnitude lower SHG. For a $500\text{-}\mu\text{m}$ thick device (double polished GaAs wafer), the SHG saturates at high irradiance accompanied with the emergence of measurable band-gap recombination radiation (photoluminescence, PL). The PL intensity scales as the third power of fundamental intensity (input peak power), which is explained by a model including three photon absorption (3PA) and free carrier absorption (FCA). For a $20\text{-}\mu\text{m}$ thick structure thinned by wet etching, the room temperature band-gap emission (BE) (PL) scales, surprisingly, as the fifth power of the fundamental intensity. This is explained as a transition from nonradiative to radiative recombination as the carrier density increases as a result of 3PA. The saturation of the SHG from nanoscale structures has implications for many applications, such as frequency shifters and signal processing for optical communications.

II. NONLINEAR SECOND HARMONIC GENERATION

A. Measurement setup

The optical setup for SHG measurement is shown in Fig. 2. A tunable optical parametric oscillator (OPO) pumped by a Ti:sapphire laser produces pulses with 200-fs duration and 70-nm linewidth at a 1 kHz repetition rate. The signal ($1.2 \mu\text{m}$) beam is blocked by a long-pass filter ($>1.5 \mu\text{m}$). The idler ($2.1 \mu\text{m}$) beam is focused to a diameter of $\sim 300 \mu\text{m}$ on the sample mounted in an optical cryostat. The sample is oriented with the substrate facing the incident beam and the plasmonic structure facing the detector so that the SH signal is not absorbed in the substrate. The SH signal is separated from fundamental light by a short-pass filter and focused into a compact monochromator, then into a New Focus model 2153 femtoWatt InGaAs photoreceiver sensitive between 800 and 1700 nm. The optical numerical aperture is limited by the $f/8$

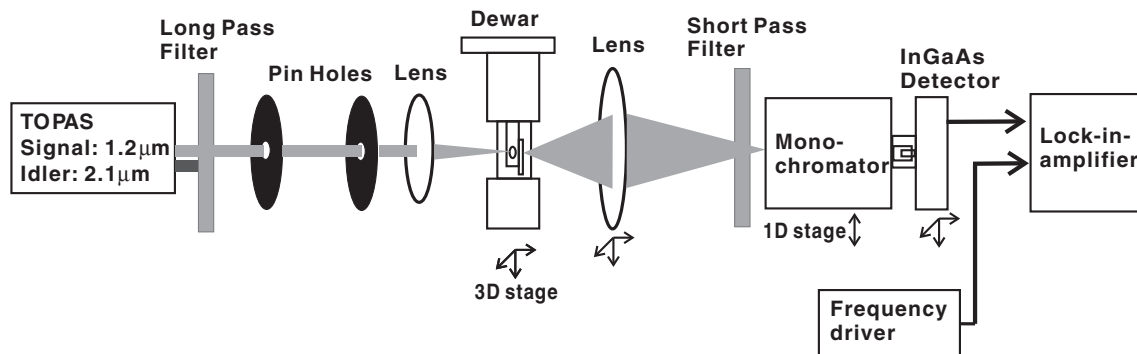


FIG. 2. Optical measurement setup.

collection lens in front of the monochromator. The spot size is varied to control the incident fluence by adjusting the position of the focusing lens in front of the cryostat along the optical axis. The detected signal and laser driving frequency are both input into a lock-in amplifier for synchronous detection. A HeNe laser is used to set the sample orientation normal to the input beam by overlapping of the reflected light and incident light through two pinholes. All measurements were carried out at normal incidence.

B. SHG measurement

An unpatterned 500 μm thick GaAs substrate with the same orientation (100) and thickness as the plasmonic sample was mounted in the Dewar. At 4 GW/cm^2 input peak power and room temperature, the sample was aligned for minimum SH generation to set normal incidence for the crystal-orientation-dependent GaAs SH signal.¹⁹ The GaAs substrate was then replaced with the patterned sample which was set to the same normal incidence direction using the alignment HeNe laser beam and the pinholes. Compared with the SHG signal of the GaAs substrate marked by empty triangles, that of the plasmon-coupled sample marked in empty squares is dramatically enhanced by the nanostructure and fit to a Gaussian spectral distribution as shown in Fig. 3(a). The wavelength of the SHG signal at 1.045 μm is half that of the 2.09 μm fundamental wavelength as required. The polarization direction of SHG from GaAs filled metallic sample is perpendicular to that of fundamental light $\vec{P}_\omega \perp \vec{P}_{2\omega}$ which is consistent with Eq. (1) resulting from the nonlinear symmetry of the GaAs material. The well-defined polarization of the SH signal confirms that the SHG is from the GaAs/plasmonics structure rather than from any roughness on the top surface of the metal.

At 297 K, as the fundamental wavelength is tuned from 1.9 to 2.3 μm , the linewidth, and the integrated SHG intensity normalized to the square of the input fluence, is obtained as a function of the input wavelength. The SHG spectra at 4 and 40 GW/cm^2 input peak power are shown in Fig 3(b). The solid line is a portion of the linear transmission curve corresponding to SPWs (1.88 μm) coupled to the first order localized mode (2.19 μm). With 4 GW/cm^2 input peak power, near the peak wavelength of the transmission, a strong SH signal is generated by the plasmon-coupled GaAs sample. As the fundamental pump wavelength is scanned away from the peak position, the corresponding SHG intensity drops at a much faster rate than the linear transmission reflecting the expected nonlinear response. The strongest SHG signal is at 1.045 μm with a 2.09 μm incident wavelength. The small blue shift of the SHG spectrum (from 2.19 to 2.09 μm) is explained by a simple point dipole theory.¹⁸ As the fundamental intensity increases to 40 GW/cm^2 at the same peak wavelength, the SHG signal is significantly broadened and distorted, reflecting a saturation of the SHG. The two SHG signals are normalized to the same peak value to allow easy comparison of the lineshapes.

To confirm that this phenomenon was due to SHG saturation and not to damage of the sample, the SHG signal power dependence was repeated for both increasing and decreasing input powers at a 2.09- μm wavelength. As shown in Fig. 4, at low input peak power 8.8 GW/cm^2 , only the SHG signal

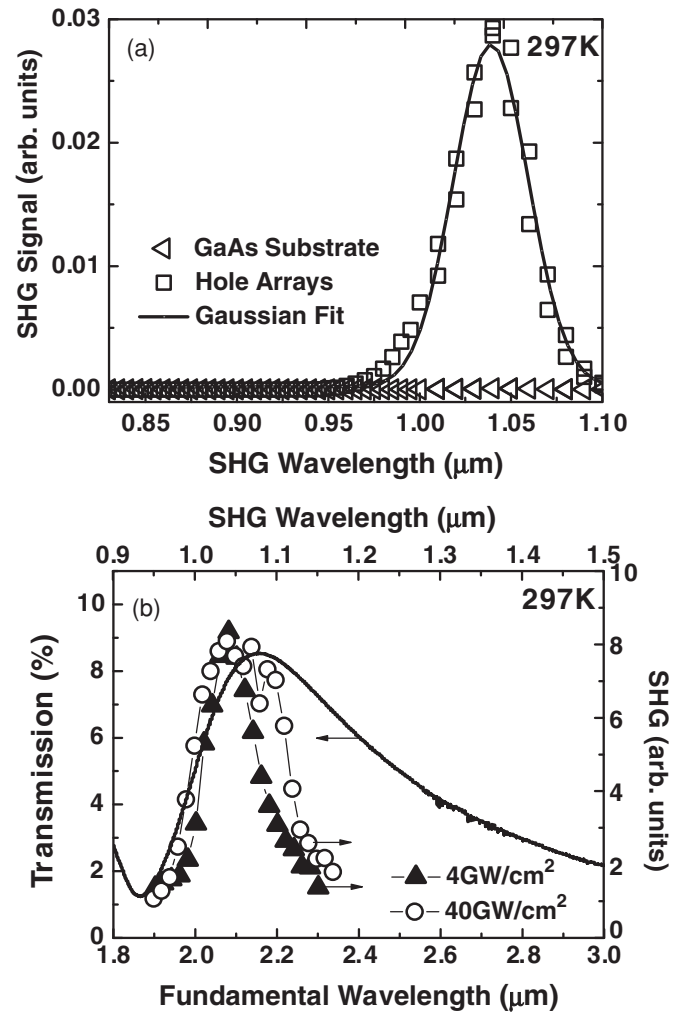


FIG. 3. (a) Contrast of the SHG signals of GaAs substrate (empty triangle marks) and of Gaussian fitting (solid line) plasmon coupled GaAs hole arrays (empty square marks) at normal incidence. (b) The peak intensity normalized wavelength-dependent SH signal spectra with 4 GW/cm^2 fundamental peak power (solid triangles) and with 40 GW/cm^2 fundamental peak power (empty circles) are confined by linear transmission spectrum (solid line).

at 1.045 μm is observed. With increased input power, in addition to the SHG signal, band-gap emission (BE or PL) appears at 890 nm, with a spectrum independent of the fundamental wavelength and monotonically increasing with the input fluence. The BE and SH signals are repeatable as the fundamental fluence is decreased, suggesting that the saturation is not due to irreversible material damage. The blue shift of the SHG response with increasing power density may be due to the contribution of the excited free carriers to the local refractive index of the GaAs.

The output SH and BE response is spectrally integrated and plotted versus the 2.09 μm input fundamental intensity in Fig. 5. For the GaAs substrate at low input peak power ($<10 \text{ GW}/\text{cm}^2$), no SH signal was observed. Due to the weak focusing associated with the experimental arrangement (deviation from a plane wave), a weak SH signal was observed at higher input peak powers with a slope of 1.1. The 890 nm

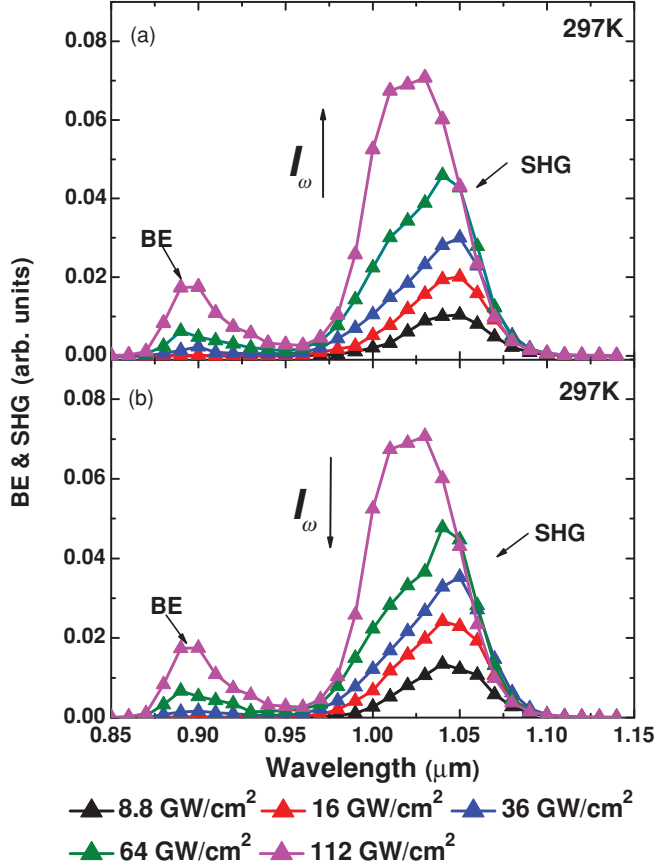


FIG. 4. (Color online) BE (~ 890 nm) and SH signal (~ 1.045 nm) with (a) increasing input peak power and then (b) decreasing input peak power at room temperature.

BE signal increases as the third power of the fundamental fluence. For plasmon coupled hole arrays, the SHG exhibits the expected quadratic power law dependence $I_{2\omega} \propto I_{\omega}^2$ at low input power, then saturates for input intensities above 10 GW/cm 2 and follows a slope of ~ 0.74 . The BE signal appears at incident intensities coincident with the saturation of the SHG with a slope of 2.8. The free carrier generation across the GaAs band gap may be due to two photon absorption (TPA) of one fundamental frequency (ω) photon and one SH frequency (2ω) photon, or by 3PA at the fundamental frequency.

C. Modeling of SHG saturation

The weakly focused ultrashort laser pulses (~ 200 fs) lead to a high peak intensity, which not only increases SH conversion efficiency also induces other nonlinear phenomena. The 297 K band gap of GaAs is 1.42 eV. 3PA of fundamental light at 2.09 μm ($E_{3\text{PA}} = 1.78$ eV), TPA of a fundamental 2.09 μm photon ($E_{1\text{PA}} = 0.59$ eV) and a SH photon at 1.045 μm ($E_{2\text{PA}} = 1.19$ eV), and FCA are the main nonlinear processes that deplete the fundamental and therefore the SH signals. The rate equations related to incident pulse [in Eq. (2)], SHG [in Eq. (3)], carrier generation [in Eq. (4)], fundamental depletion [in Eq. (5)], and SH depletion [in Eq. (6)] are expressed as

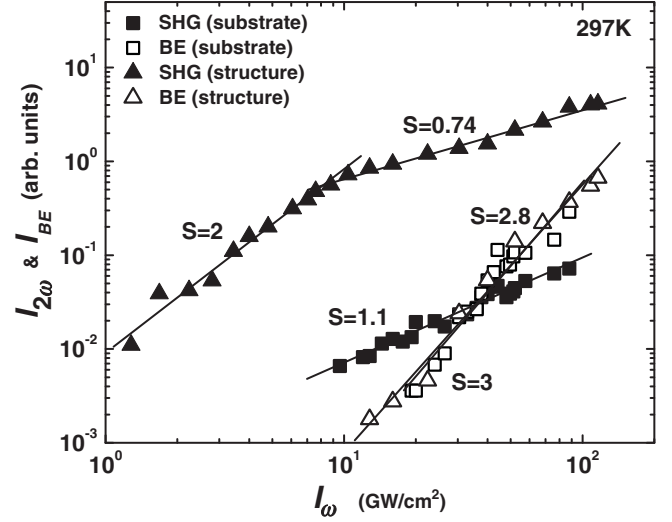


FIG. 5. At 297 K, for a GaAs substrate, SHG (in solid square makers, $I_{2\omega} \propto I_{\omega}^{1.1}$) and BE (in unfilled square marks, $I_{BE} \propto I_{\omega}^3$) intensity vs input peak power; and for plasmon-coupled structure, SHG (in solid triangles, $I_{2\omega} \propto I_{\omega}^2$ at low peak power and $I_{2\omega} \propto I_{\omega}^{0.74}$ at high peak power) and BE (in unfilled triangles, $I_{BE} \propto I_{\omega}^{2.8}$) intensity vs input peak power (log-log plots).

follows:

$$I_{\omega}(t) = I_0 \exp \left[-4 \ln(2) \frac{t^2}{\tau^2} \right], \quad (2)$$

$$\begin{aligned} I_{2\omega}(t) &= \frac{\rho^{\text{SHG}} K^{\text{SHG}}(\omega, \omega)}{\hbar \omega} I_{\omega}^2 \\ &\equiv \frac{\omega^2 L^2 |\chi_{14}^{(2)}|^2}{n_{2\omega} n_{\omega}^2 c^3 \epsilon_0} \rho^{\text{SHG}} \sin^2(\Delta k L / 2) I_{\omega}^2 \\ &\cong \frac{\omega^2 L^2 |\chi_{14}^{(2)}|^2}{n_{2\omega} n_{\omega}^2 c^3 \epsilon_0} \rho^{\text{SHG}} I_{\omega}^2, \end{aligned} \quad (3)$$

$$\begin{aligned} \frac{dN_e}{dt} &= \rho^{3\text{PA}} \frac{K^{3\text{PA}}(\omega, \omega, \omega)}{3\hbar \omega} I_{\omega}^3 + \rho_{\omega, 2\omega}^{2\text{PA}} \frac{2K^{2\text{PA}}(\omega, 2\omega)}{3\hbar \omega} \\ &\times I_{\omega} I_{2\omega} - \frac{N_e}{T_1}, \end{aligned} \quad (4)$$

$$\begin{aligned} \frac{n_{\omega}}{c} \frac{\partial}{\partial t} I_{\omega}(t) &= -\rho^{3\text{PA}} K^{3\text{PA}}(\omega, \omega, \omega) I_{\omega}^3 - [\sigma_e(\omega) + \sigma_h(\omega)] N_e I_{\omega} \\ &- \rho^{\text{SHG}} K^{\text{SHG}}(\omega, \omega) I_{\omega}^2 - 2\rho_{\omega, 2\omega}^{2\text{PA}} K^{2\text{PA}}(\omega, 2\omega) I_{\omega} I_{2\omega}, \end{aligned} \quad (5)$$

$$\begin{aligned} \frac{n_{2\omega}}{c} \frac{\partial}{\partial t} I_{2\omega}(t) &= \rho^{\text{SHG}} K^{\text{SHG}}(\omega, \omega) I_{\omega}^2 \\ &- [\sigma_e(2\omega) + \sigma_h(2\omega)] N_e I_{2\omega} \\ &- 2\rho_{\omega, 2\omega}^{2\text{PA}} K^{2\text{PA}}(\omega, 2\omega) I_{\omega} I_{2\omega}, \end{aligned} \quad (6)$$

where

$$\begin{aligned} \rho^{\text{SHG}} &\equiv \frac{1}{\text{Area} \times I_{\omega}^2(t)} \iint_{\text{unit cell}} |E_x(x, y; t) \\ &\times E_z(x, y; t)|^2 dx dy; \end{aligned} \quad (7)$$

$$\rho^{3PA} \equiv \frac{1}{Area \times I_{\omega}^3(t)} \iint_{\text{unit cell}} |\vec{E} \cdot \vec{E}|^3 dx dy; \quad (8)$$

$$\rho_{\omega,2\omega}^{2PA} \equiv \frac{1}{Area \times I_{\omega}^3(t)} \iint_{\text{unit cell}} |E_y(x,y;t) \times (E_x(x,y;t)E_z(x,y;t))| dx dy. \quad (9)$$

The ρ 's are geometrical factors accounting for the field enhancement and redistribution on interaction with the plasmonic structure and are defined in Eqs. (7) through (9). $\rho^{\text{SHG}} = 1.23$ (compared to zero for a bulk crystal by symmetry), $\rho^{3PA} = 3.8 \times 10^4$, and $\rho_{\omega,2\omega}^{2PA} = 0.013$.

We assume the input pulse has a Gaussian temporal shape with FWHM τ [Eq. (2)]²⁰. Because the active thickness of the plasmonic structure Th is only around 100 nm ($nTh/C \sim 2$ fs $\ll \tau \sim 200$ fs), we can ignore the variation along the pulse propagation direction so the SHG simply follows the square of the input pulse in time. Since the active region is much shorter than the GaAs phase matching coherence length $\Delta kL \ll 1$, the SH signal is generated as Eq. (3) by setting the *sinc* function to unity, $\sin c(\frac{\Delta kL}{2}) = 1$. The refractive indexes at the fundamental and SH wavelengths are 3.34 and 3.49, respectively.

Excited carriers, $N_e = N_h$, the number of occupied states in the conduction band and unoccupied states in the valence band, as expressed by Eq. (4), where I_{ω} is the laser irradiance (W/cm²), result from 3PA of $3\hbar\omega$ (1.78 eV), from TPA of a fundamental ($\hbar\omega$), and a SH ($2\hbar\omega$) photon, and from carrier recombination and diffusion. We assume that the carriers are uniformly distributed and that there is no recombination during the laser pulse. The nonlinear absorption coefficient of 3PA K^{3PA} is 3×10^{-19} cm³/W² (Refs. 21,22), and the TPA coefficient K^{2PA} is 3×10^{-9} cm/W approximately in the near IR.²³ For a pulse with peak intensity $I_{\omega} = 5$ GW/cm², the accumulated carrier density of $\sim 10^{20}$ cm⁻³ due to 3PA is much higher than the carrier density of $\sim 10^{11}$ cm⁻³ caused by TPA of fundamental and SH light, because the SH conversion efficiency is still quite low $\sim 10^{-5}$. The carrier density caused by the second term can be neglected. Given the fs-time scale of the pulse, recombination is ignored [e.g., the third term on the right-hand side of Eq. (4) is set to zero for calculating the carrier concentration during the laser pulse]. The refractive index decrease resulting from the 3PA induced carrier density is the reason that the SHG peak blue shifts with the increase of fundamental intensity as shown in Fig. 4.

The rate equation for the depletion of the fundamental intensity is given in Eq. (5). One-photon and two-photon absorption of fundamental light are not of concern since $\hbar\omega, 2\hbar\omega < E_g$. The first and second terms on the right-hand side represent the depletion caused by 3PA and FCA. The third and fourth terms represent the depletion resulting from SHG and TPA of ω and 2ω , which can be ignored due to the low SHG conversion efficiency. The second order susceptibility $\chi_{GaAs}^{(2)}$ is $3.46 \cdot 10^{-8}$ cm/V at a 2.1 μm wavelength.^{15,24} Both the electron and the hole absorption cross sections are included, but dipole-allowed transitions from the heavy- to the light-hole bands are by far the strongest component of FCA and of the total nonlinear loss. Intraband transitions in the conduction

band are indirect and much weaker.²⁵ Therefore, it is the absorption by heavy holes generated as a result of 3PA driving the carrier concentration that drives the saturation. The irradiance-independent hole cross section is $\sigma_H = 1 \times 10^{-16}$ cm² (Ref. 26).

The rate equation for the depletion of the SH light is given by Eq. (6). In addition to the depletion of the fundamental expressed as the first term, FCA at 2ω , expressed in the second term, is another factor which limits the SH conversion efficiency. However, due to the low SH conversion efficiency, 2PA of 2ω and ω , the third term, does not contribute significantly.

Since the fundamental intensity and the SH intensity interact with each other, these equations are coupled and were solved numerically. For the calculation, a time step of 1 fs was used, much shorter than the photon transit time through the ~ 100 -nm thick GaAs active region. The laser pulse I_{ω} is depleted due to the 3PA, generating free carriers which in turn reduce both I_{ω} and $I_{2\omega}$ by FCA. We used a finite-difference time-domain (FDTD) numerical method for the analysis of TPA, FCA, and SHG which has been presented in Refs. 27,28.

The calculated fundamental transmission and SH temporal pulse shapes, with and without absorption, are plotted in Fig. 6. As shown in Fig. 6(a), the input pulse at fundamental wavelength with $I_0 = 5$ GW/cm² is plotted with a black solid line; the fundamental pulse transmitted through the GaAs sample, depleted as a result of only the 3PA, is shown as a red dashed line; the transmitted pulse depleted by 3PA and FCA is plotted as the blue dash-dot line. The SH pulses corresponding to the fundamental depletions are plotted with the same line style convention in Fig. 6(b). The SH intensity introduces an additional FCA giving the additional depletion seen in the green dotted line.

Integrating the pulse over time gives a straightforward explanation for the experimental results. The transmission from two lenses ($\sim 85\%$), two windows of the cryostat ($\sim 85\%$) and other scattering factors in the optical setup, and the transmission through the vacuum/GaAs interface ($\sim 65\%$) account for only $\sim 47\%$ transmission to the active region. The simulated transmitted fundamental intensity versus the input intensity without absorption, with 3PA of the fundamental intensity, and with 3PA and FCA depletion of the fundamental intensity are plotted in Fig. 7(a); the corresponding SHG intensity and the additional depletion of the SHG resulting from FCA versus the fundamental intensity are plotted in Fig. 7(b). The fundamental intensity in experimental plots in Fig. 5 ranges from 1 to 100 GW/cm², while that in the simulation plots in Fig. 7(b) ranges from 0.1 to 100 GW/cm². The SH saturates at a fundamental intensity of ~ 1 GW/cm² in the simulation plots, while the SH saturates at a fundamental intensity 10 GW/cm² in the experimental plots. The accuracy of the many coefficients needed for the simulation, and the sensitivity threshold of the detection system may cause some differences between the modeled and experimentally determined threshold intensity for SHG saturation. Experimentally, the SH units are arbitrary. Compared with the simulation and experimental results, especially the SHG saturation with fundamental intensity ranging from 1 to 10 GW/cm² in Fig. 7(b) and from 10 to 100 GW/cm² in Fig. 5, we conclude that 3PA and FCA of fundamental wavelength are the main factors

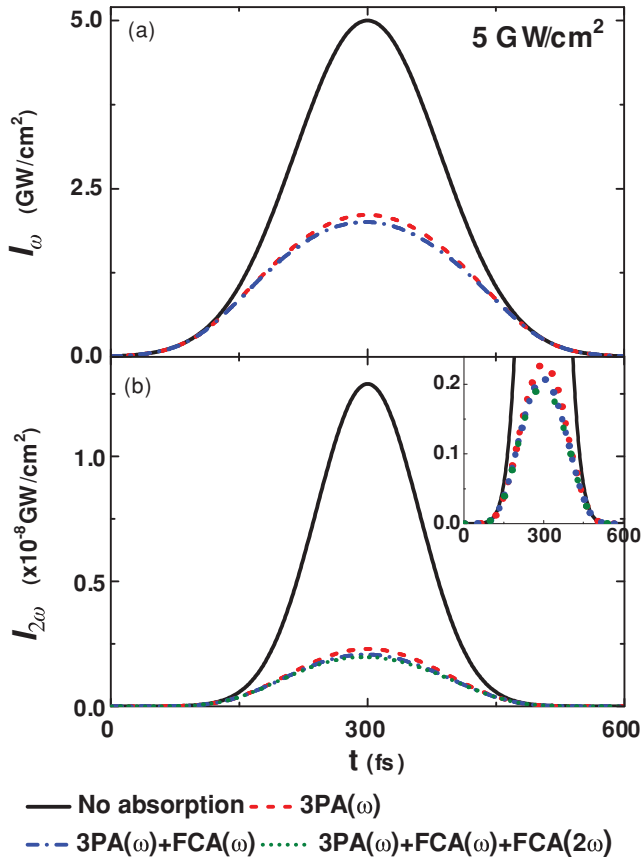


FIG. 6. (Color online) For fundamental pulse peak intensity of 5 GW/cm^2 , (a) the fundamental pulse without absorption (black solid line), with 3PA (red dashed line), with 3PA and FCA at ω (blue dash dotted line); (b) the SH pulse due to fundamental signal without absorption (black solid line), with 3PA (red dashed line), 3PA and FCA at ω (blue dash dotted line), and with FCA at 2ω additionally (green dotted line). The inset emphasizes the SHG depletion by 3PA and FCA at ω and 2ω .

that cause the SHG saturation, limiting the SH conversion efficiency, and introducing additional band-gap emission. The SHG saturation will be significantly impacted by FCA when the fundamental intensity is increased by another order of magnitude in Fig. 7(b), which is beyond our measurement range (100 to 1000 GW/cm^2). The SHG of course follows the input pulse, in contrast the BE time scale is given by the much longer carrier recombination times. Since the carrier generation is a three photon process, the BE scales as the cube of the fundamental intensity.

In addition to the processes discussed above, nonlinear refractive effects may also influence the results.^{29,30} A bistable transmission is predicted for intensities on a scale comparable to those of this experiment. For GaAs, the nonlinear refractive index is $n_2 \sim 1.3 \times 10^{-4} \text{ cm}^2/\text{GW}$ (Ref. 22) and at our peak intensities, $n_2 I_\omega \sim 10^{-3}$ to 10^{-2} , a level at which nonlinear refractive effects are predicted. This nonlinearity is likely overwhelmed by the contributions of the free carriers; at a density of 10^{20} cm^{-3} , the local index is depressed by up to 35%. However, the SPW coupling extends over much larger spatial scales than the localized carrier densities at the GaAs

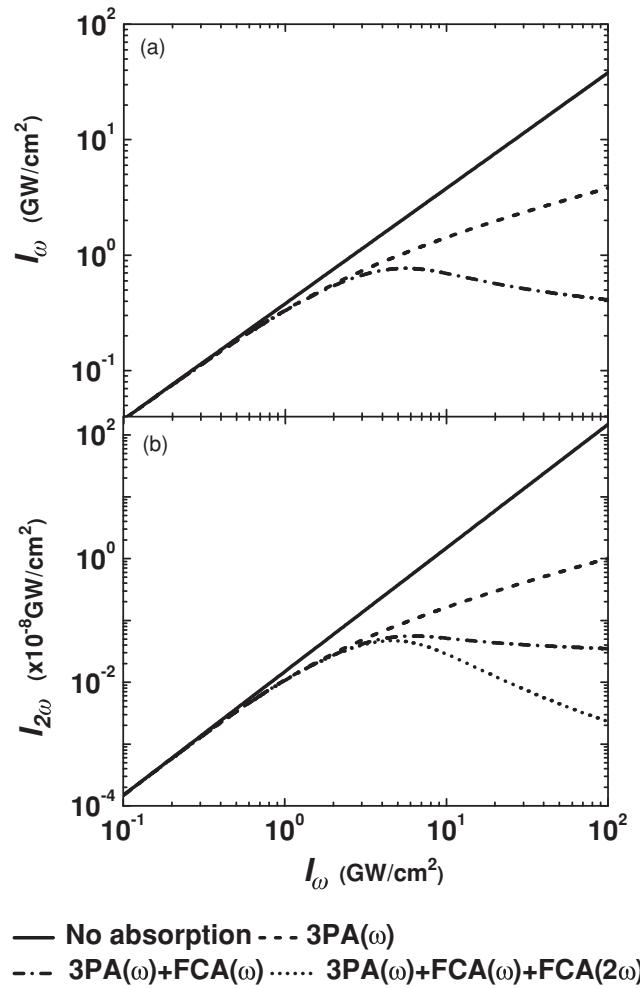


FIG. 7. (a) The simulated transmitted fundamental intensity and (b) the SH intensity exiting the GaAs active slab versus the input fundamental intensity. Solid lines represent $\sim 47\%$ transmission of fundamental light; dashed lines include 3PA at ω ; dash dotted lines represent the pulse intensity including both 3PA and FCA at ω ; and the dotted line represents the impact of the FCA on the SHG intensity.

pillars. More study is needed understand the role of these refractive effects on the observed saturation.

D. Fifth order intensity dependence of the BE from a $20 \mu\text{m}$ thick GaAs substrate

To reduce the influence of multiphoton absorption in the bulk GaAs material before the input pulse reaches the nonlinear region, a $\sim 2\text{-mm}$ diameter hole was wet etched from back side of the sample using a solution of $\text{H}_2\text{SO}_4 : \text{H}_2\text{O}_2 : \text{H}_2\text{O}$ (1:8:1). The remaining GaAs substrate under the plasmonic structure was $\sim 20\text{-}\mu\text{m}$ thick with a mirror like etched surface. We expected the reduced nonlinear absorption associated with the thinner GaAs substrate to increase the SHG conversion efficiency. However, the SHG efficiencies were comparable for the two samples. The observed room temperature BE signal, stimulated by the input peak power $>10 \text{ GW/cm}^2$, is not reduced but is significantly enhanced and displays a surprising fifth power dependence on the incident intensity, even though it arises from a 3PA process. Due to the significantly different

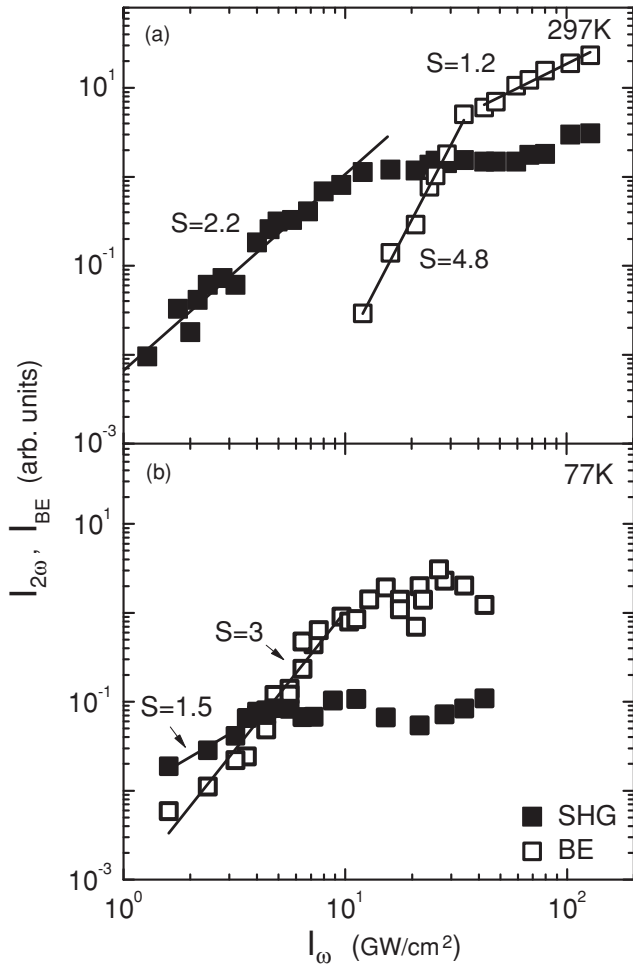


FIG. 8. (a) At 297 K, $I_{2\omega} \propto I_{\omega}^{2.2}$ (solid squares) at input peak power < 10 GW/cm 2 ; $I_{BE} \propto I_{\omega}^{4.8}$ (unfilled squares) at input peak powers < 35 GW/cm 2 and $I_{BE} \propto I_{\omega}^{1.2}$ at fundamental power > 35 GW/cm 2 . (b) At 77 K, $I_{2\omega} \propto I_{\omega}^{1.5}$ (solid squares) and $I_{BE} \propto I_{\omega}^3$ (unfilled squares) at fundamental power < 8 GW/cm 2 .

carrier scattering processes at different temperatures, the SHG and BE were studied for substrates at 297 and 77 K.

The BE and SHG spectral variation with fundamental power was repeated for both increasing and decreasing power levels, confirming that there was no sample damage at the highest fluences used. The linewidth integrated BE and SH intensities versus fundamental intensity are plotted in Figs. 8(a) and 8(b), which has the same arbitrary units as Fig. 5. At 297 K, the SHG saturates at the same threshold input peak power, ~ 10 GW/cm 2 , as for the plasmonic structure on pre-epi GaAs substrate. However, the PL intensity is strongly enhanced compared with the signal from the plasmonic structure on the pre-epi GaAs substrate. The BE power scales approximately as the fifth order of the fundamental input peak power, for input fluences less than ~ 35 GW/cm 2 , then saturates at input peak powers > 35 GW/cm 2 . At 77 K, the BE is observed at a lower input peak power (2 GW/cm 2), follows the expected cubic dependence on peak power, and then saturates as shown in Fig. 8(b). The SHG signal is weaker than at room temperature corresponding to the higher BE signal (and higher carrier concentration). Clearly, the SHG saturation is correlated with

the appearance of the BE signal. The larger BE signal in the thinned sample corresponds to a higher carrier concentration at the surface near the plasmonics structure, leading to enhanced saturation effects and qualitatively explaining the lack of improvement in the SHG efficiency for this thinned sample.

E. Modeling the intensity dependence of the BE from thin GaAs samples (~ 20 nm)

The 200-fs pulse generates carriers in the GaAs material by 3PA. The lifetime of these carriers, controlled by both radiative and nonradiative recombination processes, is much longer than the laser pulse duration. The BE measurement is sensitive to the integrated BE intensity over the carrier lifetime. The initial condition of $N(t = 0^+) = N_0$, is accumulated through 3PA process during laser pulse as modeled in Sec. II C. The carrier recombination is described by Eq. (10),

$$\begin{aligned} \frac{dN_e}{dt} &= -\frac{N_e}{\tau_{NR}} - B(N_e + n_0)(N_e + p_0) \\ &= -\left[\frac{1}{\tau_{NR}} + B(n_0 + p_0)\right]N_e - BN_e^2 = -\frac{N_e}{\tau} - BN_e^2, \end{aligned} \quad (10)$$

where n_0 and p_0 are the intrinsic electron and hole densities, N_e is the excited carrier density and B is the bimolecular recombination coefficient ($\sim 10^{-10}$ cm 3 /s for GaAs) (Ref. 31). The nonradiative recombination lifetime is τ_{NR} , low concentration radiative recombination lifetime.³² $\tau_R = 1/B(n_0 + p_0) \approx 8$ ns and $\frac{1}{\tau} \equiv \frac{1}{\tau_{NR}} + \frac{1}{\tau_R}$. The second term in Eq. (10) becomes important at high carrier concentrations and represents additional radiative recombination. It is straightforward to integrate Eq. (10) to obtain the time dependence of the excited carrier concentration in Eq. (11)

$$N_e(t) = \frac{N_0 e^{-t/\tau}}{1 + BN_0\tau(1 - e^{-t/\tau})}. \quad (11)$$

Here $N_0 \propto I_{\omega}^3$ is the carrier concentration at the end of the input pulse. From this result, the integrated intensity of the BE, S_e is readily obtained by Eq. (12)

$$S_e \propto N_0 - \int_0^{\infty} N_e(t) dt / \tau_{NR} = N_0 - \frac{\ln|1 + BN_0\tau|}{B\tau_{NR}}. \quad (12)$$

In the present sample, with patterning at the ~ 100 -nm scale, there is likely to be damage to the GaAs giving rise to a decrease in τ_{NR} compared to bulk material, and the most likely situation is that $\tau_{NR} \ll \tau_R$, so $\tau \sim \tau_{NR}$. Then in the low excitation limit, $BN_0\tau \ll 1$, and $S_e \rightarrow (\tau_{NR}/\tau_R)I_{\omega}^3$. At high excitations, $BN_0\tau > 1$, and then $S_e \rightarrow I_{\omega}^3$. In the transition between these two regimes, the dependence on the excitation level is faster than the cubic intensity dependence in the two limiting cases as a larger and larger fraction of the carriers recombine radiatively, consistent with the experimental observation of an I_{ω}^5 dependence. The variation of S_e as a function of τ_{NR} for three different excitation levels (N_0) is shown in Fig. 9(a). For very short τ_{NR} , the signal is proportional to τ_{NR} with different offsets related to the increasing impact of bimolecular recombination at higher excitation levels. As τ_{NR} increases, the output saturates at

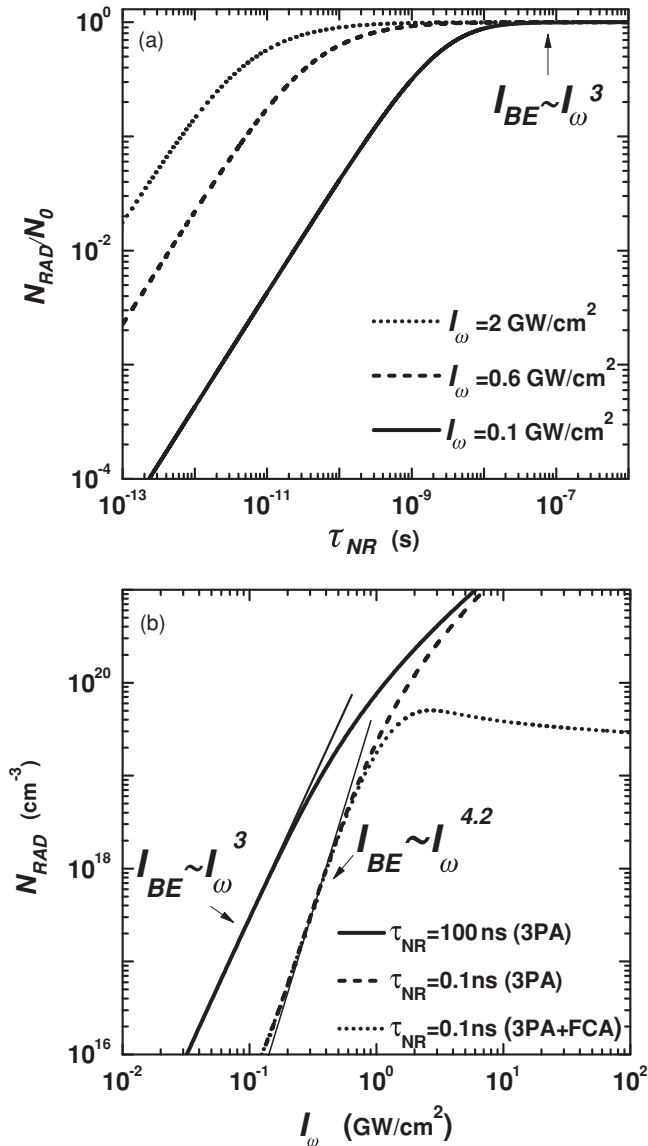


FIG. 9. (a) The nonradiative recombination lifetime τ_{NR} dependence of the ratio of carrier density of radiative recombination over total carrier density N_{RAD}/N_0 with input power 0.1, 0.6, and 2 GW/cm^2 . (b) The radiative recombination carrier density vs. input peak power with τ_{NR} 100 ns, 0.1 ns with fundamental light depleted by 3PA, and 0.1 ns with fundamental light depleted by 3PA and FCA

$N_0 \propto I_\omega^3$ as the recombination is dominated by bimolecular radiative processes.

In Fig. 9(a), the carrier density versus the fundamental input peak power is plotted with τ_{NR} as a parameter. This

simulation plot explains the experimentally observed I_ω^5 BE dependence. Here, the initial excited carrier density N_0 , is the time integral of Eq. (4) as a function of I_ω and $I_{2\omega}$ with 3PA and FCA depletion. At room temperature, the intensity of the BE scales as the third power of the input intensity for intensities $< 0.3 \text{ GW}/\text{cm}^2$, and then saturates due to depletion of the fundamental by free-carrier absorption. However, for a thinned GaAs substrate, the intensity dependence of the BE is $\sim I_\omega^{4.2}$ at input peak powers ranging from ~ 0.1 to $\sim 0.4 \text{ GW}/\text{cm}^2$, saturating at higher powers, agreeing well with the experimental BE results for the plasmonic structure on a thinned GaAs membrane as shown in Fig. 8(a). This corresponds to the model calculation as shown in the plot of Fig. 9(b). The low excitation BE corresponds to the additional FCA of the pump light, the BE intensity saturates at a lower threshold input peak power with more loss at the same τ_{NR} . Here the simulation gives $\text{BE} \sim I_\omega^{4.2}$. Without the influence of the depletion of the fundamental, an I_ω^5 or even higher order (> 5) intensity dependence is calculated. At 77K, the τ_{NR} is increased until radiative recombination dominates, and the BE intensity scales as the third power of the incident intensity, coinciding with the experimental data as shown in Fig. 8(b).

III. CONCLUSION

Plasmon-enhanced nonlinear optics offers field concentration enhancing nonlinear optical processes. For SHG, the interaction length is short ($\sim 100 \text{ nm}$), and phase matching is not required. The polarization direction of SH is perpendicular to that of fundamental light, $\vec{E}_{2\omega} \perp \vec{E}_\omega$, which is consistent with the symmetry of the GaAs $\chi_{14}^{(2)}$. The SHG is strongly enhanced over any residual, symmetry-forbidden signal from bulk GaAs, and saturates due to FCA arising from 3PA generated carriers in a bulk GaAs substrate ($500 \mu\text{m}$) with the BE scaling as the cube of the input light intensity. For a thinned sample with the excitation confined more closely to the plasmonic region, a surprising fifth-order dependence of the BE on the input power is observed for a fundamental frequency close to $1/3$ of the band-gap frequency at room temperature, resulting from the transition from nonradiative to bimolecular radiative-dominated carrier recombination.

ACKNOWLEDGMENT

We acknowledge useful discussions with Dr. Michael P. Hasselbeck. This work was supported by DARPA as part of the University Photonics Centers Program.

*Corresponding author: sbrueck@chtm.unm.edu

¹H. Raether, *Surface Plasmons on Smooth and Rough Surfaces and on Gratings*, (Springer-Verlag, New York, 1988).

²T. W. Ebbesen, H. J. Lezec, H. F. Ghaemi, T. Thio, and P. A. Wolff, *Nature (London)* **391**, 667 (1998).

³S. Zhang, W. Fan, N. C. Panoiu, K. J. Malloy, R. M. Osgood, and S. R. J. Brueck, *Phys. Rev. Lett.* **95**, 137404 (2005).

⁴J. Zhang, S. Zhang, D. Li, A. Neumann, C. Hains, A. Frauenglass, and S. R. J. Brueck, *Opt. Exp.* **15**, 8737 (2007).

⁵Z. Ku, J. Zhang, and S. R. J. Brueck, *Opt. Exp.* **17**, 6782 (2009).

⁶W. Fan, S. Zhang, B. Minhas, K. J. Malloy, and S. R. J. Brueck, *Phys. Rev. Lett.* **94**, 033902 (2005).

⁷A. Bouhelier, M. Beversluis, A. Hartschuh, and L. Novotny, *Phys. Rev. Lett.* **90**, 013903 (2003).

- ⁸K. Chen, C. Durak, J. R. Heflin, and H. D. Robinson, *Nano Lett.* **7**, 254 (2007).
- ⁹A. Nahata, E. A. Linke, T. Ishi, and K. Ohashi, *Opt. Lett.* **28**, 423 (2003).
- ¹⁰S. I. Bozhevolnyi, J. Beermann, and V. Coello, *Phys. Rev. Lett.* **90**, 197403 (2003).
- ¹¹A. M. Moran, J. Sung, E. M. Hicks, R. P. Van Duyne, and K. G. Spears, *J. Phys. Chem. B* **109**, 4501 (2005).
- ¹²B. K. Canfield, H. Husu, J. Laukkanen, B. Bai, M. Kuittinen, J. Turunen, and M. Kauranen, *Nano Lett.* **7**, 1251 (2007).
- ¹³J. A. H. Van Nieuwstadt, M. Sandtke, R. H. Harmsen, F. B. Segerink, J. C. Prangsma, S. Enoch, and L. Kuipers, *Phys. Rev. Lett.* **97**, 146102 (2006).
- ¹⁴F. B. P. Niesler, N. Feth, S. Linden, J. Niegemann, J. Gieseler, K. Busch, and M. Wegener *Opt. Lett.* **34**, 1997 (2009).
- ¹⁵T. Skauli, K. L. Vodopyanov, T. J. Pinguet, A. Schober, O. Levi, L. A. Eyres, M. M. Fejer, and J. S. Harris *Opt. Lett.* **27**, 628 (2002).
- ¹⁶E. J. Lim, M. M. Fejer, and R. L. Byer, *Electron. Lett.* **25**, 174 (1989).
- ¹⁷W. Fan, S. Zhang, K. J. Malloy, and S. R. J. Brueck, *Opt. Exp.* **14**, 9570 (2006).
- ¹⁸W. Fan, S. Zhang, N. C. Panoiu, A. Abdenour, S. Krishna, R. M. Osgood, K. J. Malloy, and S. R. J. Brueck, *Nano Lett.* **6**, 1027 (2006).
- ¹⁹R. W. Boyd, *Nonlinear Optics*, (Elsevier New York, 2003), Chap. 2.
- ²⁰R. Schroeder and B. Ullrich, *Opt. Lett.* **27**, 1285 (2002).
- ²¹J. U. Kang, A. Villeneuve, M. Sheik-Bahae, and G. I. Stegeman, *Appl. Phys. Lett.* **65**, 147 (1994).
- ²²W. C. Hurlbut, Y.-S. Lee, K. L. Vodopyanov, P. S. Kuo, and M. M. Fejer, *Opt. Lett.* **32**, 668 (2007).
- ²³T. G. Ulmer, R. K. Tan, Z. Zhou, S. E. Ralph, R. P. Kenan, and C. M. Verber, *Opt. Lett.* **24**, 756 (1999).
- ²⁴O. Madelung, U. Rössler, and M. Schulz, in *Group IV Elements, IV-IV and III-V Compounds Part a*, Landolt-Börnstein Database Vol. 41A1a, (Springer-Verlag, 2001).
- ²⁵M. P. Hasselbeck, E. W. Van Stryland, and M. Sheik-Bahae, *J. Opt. Soc. Am. B* **14**, 1616 (1997).
- ²⁶R. Braunstein and E. O. Kane, *J. Phys. Chem. Sol.* **23**, 1423 (1962).
- ²⁷A. F. Gibson, C. B. Hatch, P. N. D. Maggs, D. R. Tilley, and A. C. Walker, *J. Phys. C: Solid State Phys.* **9**, 3259 (1976).
- ²⁸N. Suzuki, *J. Lightwave Technol.* **25**, 2495 (2007).
- ²⁹J. A. Porto, L. Martin-Moreno, and F. J. Garcia-Vidal, *Phys. Rev. B* **70**, 081402(R) (2004).
- ³⁰S. Carretero-Palacios, A. Minovich, D. N. Neshev, Y. S. Kivshar, F. L. Garcia-Vidal, L. Martin-Moreno, and S. G. Rodrigo, *Opt. Lett.* **35**, 4211 (2010).
- ³¹L. A. Coldren and S. W. Corzine, *Diode Lasers and Photonic Integrated Circuits*, (John Wiley & Sons, New York, 1995), Chap. 1.
- ³²T. Nakano and T. Oku, *Jpn. J. Appl. Phys.* **6**, 1212 (1967).